



HAL
open science

Sensitivity to welding positions and parameters in GTA welding with a 3D multiphysics numerical model

Minh Chien Nguyen, Marc Medale, Olivier Asserin, Stephane Gounand,
Philippe Gilles

► **To cite this version:**

Minh Chien Nguyen, Marc Medale, Olivier Asserin, Stephane Gounand, Philippe Gilles. Sensitivity to welding positions and parameters in GTA welding with a 3D multiphysics numerical model. Numerical Heat Transfer, Part A Applications, 2017, 71 (3), pp.233 - 249. 10.1080/10407782.2016.1264747 . hal-01791099

HAL Id: hal-01791099

<https://amu.hal.science/hal-01791099>

Submitted on 11 Jun 2021

HAL is a multi-disciplinary open access archive for the deposit and dissemination of scientific research documents, whether they are published or not. The documents may come from teaching and research institutions in France or abroad, or from public or private research centers.

L'archive ouverte pluridisciplinaire **HAL**, est destinée au dépôt et à la diffusion de documents scientifiques de niveau recherche, publiés ou non, émanant des établissements d'enseignement et de recherche français ou étrangers, des laboratoires publics ou privés.



Distributed under a Creative Commons Attribution - NonCommercial - NoDerivatives 4.0
International License

Sensitivity to welding positions and parameters in GTA welding with a 3D multiphysics numerical model

Minh Chien NGUYEN^{1,2}, Marc MEDALE², Olivier ASSERIN¹,
Stephane GOUNAND¹ and Philippe GILLES³

¹Den-SEMT, CEA, Université Paris-Saclay, F-91191, Gif-sur-Yvette, France
(minhchienxf@gmail.com, olivier.asserin@cea.fr, stephane.gounand@cea.fr)

²Aix Marseille University, IUSTI, UMR 7343 CNRS, F-13453, Marseille, France
(marc.medale@univ-amu.fr)

³AREVA, F-92084, Paris La Défense, France
(philippe.gilles@areva.com)

Mailing address of the corresponding author: *Minh Chien NGUYEN, Den-SEMT, CEA, Université Paris-Saclay, F-91191, Gif-sur-Yvette, France*

Short title for running head: *A 3D multiphysics numerical model of GTA welding*

Abstract

A 3D numerical model of Gas Tungsten Arc welding has been developed to predict weld bead shape, fluid flow in the weld pool as well as thermal field in the workpiece. This model accounts for coupled electromagnetism, heat transfer and fluid flow with a moving free surface to simulate different welding positions. The solution strategy of the coupled non-linear equations that has been implemented in the Cast3M finite element code is also discussed. The capabilities of our numerical model are first assessed by comparison to experimental results. Then, as fluid flows in weld pool play a prominent role in the weld quality as well as in the final shape of the weld bead seam, the effect of various welding positions on the weld pool shape has been investigated which constitutes the main novelty of this work. The performed computations point out a strong sensitivity to gravity on the weld pool shape depending on assisting or opposing weld direction with respect to gravity. This study contribute to assess the model capabilities in providing a deeper physical insight towards a more efficient optimization of welding processes.

Keywords: GTAW simulations, multiphysics, welding positions, weld pool, Cast3M.

Nomenclature

\mathbf{A}	magnetic vector potential, T·m
\mathbf{B}	magnetic induction, T
\mathbf{E}	electric field, V·m ⁻¹
\mathbf{f}_{Arc}	arc pressure, N·m ⁻²
\mathbf{f}_{Body}	gravity force, N·m ⁻³
\mathbf{f}_{Ext}	velocity extinction force, N·m ⁻³
\mathbf{f}_{Lor}	Lorentz force, N·m ⁻³
\mathbf{f}_{Mar}	Marangoni force, N·m ⁻²
\mathbf{j}	electric current density, A·m ⁻²
\mathbf{n}	normal vector
\mathbf{s}_{Cvs}	convective heat loss, W·m ⁻²
\mathbf{s}_{Ray}	radiation loss, W·m ⁻²
\mathbf{s}_{Sur}	surface heat source, W·m ⁻²
$\mathbf{t}_1, \mathbf{t}_2$	tangent vectors
\mathbf{u}	flow velocity, m·s ⁻¹
\mathbf{u}_s	welding speed, m·s ⁻¹
c	constant
c_p	specific heat, J·kg ⁻¹ ·K ⁻¹
f_l	liquid metal fraction
g	gravity, m·s ⁻²
h	enthalpy per unit mass, J·kg ⁻¹
h_c	convective heat transfer coeff., W·m ⁻² ·K ⁻¹
I	total electric current, A
L	latent heat, J·kg ⁻¹
p	pressure in the liquid phase, N·m ⁻²
p_{max}	maximum arc pressure, N·m ⁻²
r_p	radius of the arc pressure, mm
r_q	radius of the heat source, mm
r_ϕ	radius of the electric curre, mm
s_{Joule}	Joule effect, W·m ⁻³
T	temperature field, K
U	voltage, V
β	thermal expansion coefficient, K ⁻¹
γ	surface tension, N·m ⁻¹
ϵ	radiation emissivity
η	process efficiency
λ	thermal conductivity, W·m ⁻¹ ·K ⁻¹
μ	dynamic viscosity, kg·m ⁻¹ ·s ⁻¹
μ_0	magnetic permeability, H·m ⁻¹
ρ	density, kg·m ⁻³
σ	electrical conductivity, S·m ⁻¹
σ_B	Stefan-Boltzmann constant, W·m ⁻² ·K ⁻⁴
ϕ	electric scalar potential, V

1 Introduction

Gas Tungsten Arc (GTA) welding is a joining process in which local melting of workpieces to be assembled is obtained by an electric arc, leading to the simultaneous presence of solid and liquid metal together with an arc plasma. It produces high quality welds for most metals and is widely used in both manual and robotic welding. However, welding metal components could be a limiting stage in many assembly designs as the integrity of the final product depends on the weld strength. Moreover, the quality of welds is partly determined by the weld pool geometry, whose shape can be significantly influenced by process parameters and operating conditions, especially in Gas Tungsten Arc (GTA) welding. Therefore, many experiments are often required to optimize the welding process for new applications but they are time consuming and costly, so numerical simulations are helpful to lower the cost of the optimization process.

Although the electric arc and resulting weld pool interact with each other very closely, a review of the literature reveals that most 3D models separately deal with arc plasma and weld pool. Indeed, the development of comprehensive multiphysics models is cumbersome and their computational times are prohibitive. In order to reduce the computational costs of fully coupled arc plasma - weld pool numerical models some authors assume an axial symmetry [1, 2, 3, 4]. But this assumption precludes to recover several important quantities such as weld pool size, since the thermal field and its related fluid flow are three dimensional. Consequently, GTA welding may not be accurately predicted unless three-dimensional computations accounting for cathode, arc plasma and anode are performed. When looking at 3D weld pool models, only few results have been published, often with restrictive assumptions. Indeed, either the surface tension gradient is fixed to a constant value [5, 6, 7] or the weld pool surface is kept flat [8, 9, 10], or the welding speed is not accounted for [7]. Accurate prediction of weldability requires a thorough knowledge of the fluid flow in the weld pool. It depends on welding parameters, material properties and thermal field as the fluid flow is mainly driven by thermal and solutal Marangoni effect [10]. Furthermore, the weld pool shape is intricately correlated to the fluid flow and weld pool surface deformation, whose shape is usually determined using either a principle of energy minimization [11, 12], free-surface tracking [3] or Volume of Fluid (VOF) method [13, 14]. To the best of the authors' knowledge, no study in the open literature presents GTA welding computations in various welding positions. Indeed, the study of Kumar and DebRoy [15] considered a tilted corner shape configuration with deformable free surface, but in Gas Metal Arc (GMA) welding, where the impact of droplets significantly deforms the free surface of melted pool. Whenever the liquid-gas interface depends on arc pressure [16] and welding position through gravity [15], most published works assume a non-deforming free surface [8, 9, 10].

In this paper a numerical model for GTA welding focusing on the weld pool is pre-

sented. It has several welding parameters as input and is able to predict relevant welding features for various configurations. Fluid flow in the weld pool results from surface tension gradient, electromagnetic force, drag force and buoyancy [17]. This model follows previous works of Brochard [4] and Kong [18] and accounts for 3D configurations with deformable free surface. In section 2, modeling assumptions and related governing equations are first presented. Then, the numerical solution procedure is described in section 3, while a comparison with an experiment is carried out to assess its capabilities in section 4. In section 5, a comprehensive parametric study that aims at investigating the influence of welding positions on the weld pool geometry, thermal field and fluid flow has been conducted. It constitutes the main novelty of this work. The results presented in this section underline the effect of gravity on the weld pool shape. Finally, a parametric study accounting for the free surface deformation is carried out to investigate the influence of the other main welding process parameters (welding speed, arc pressure and sulfur content) on the weld pool topology (section 6).

2 Governing equations

2.1 Physical model assumptions

A multiphysics model accounting for the coupling between electromagnetism, heat transfer and free-surface fluid flow in the weld pool is derived in this section. The electric arc is modeled by an electric current applied to the upper surface of the anode below the welding torch, a resulting heat flux and an induced arc pressure. The problem reduces then to the welding assembly, on which the distributions of the modeled electric arc quantities are assumed Gaussian. The welding speed is assumed constant and the problem is defined in the coordinate system attached to the torch, so that a steady solution can be seek. The electromagnetic, continuity, momentum and energy equations are solved in the weld pool, whereas only the electromagnetic and energy equations are solved in the solid. The liquid metal is assumed Newtonian, its fluid flow remains laminar and the Boussinesq's approximation is used. Moreover, depending on the welding position the considered problem can possess the longitudinal vertical median plane as symmetry plane so the computational domain consists in this case of only one half plate (figure 1).

2.2 Electromagnetic model

At steady state there is no interaction between electric and magnetic fields. Therefore, a simplified form of Maxwell's equations is considered, that splits into an electrostatic part and a magnetostatic one.

- Electrostatic part:

$$\nabla \cdot (-\sigma \nabla \phi) = 0 \quad (1)$$

with associated boundary conditions:

$$\nabla \phi \cdot \mathbf{n} = \frac{3I}{\pi r_\phi^2} \exp\left(-\frac{3r^2}{r_\phi^2}\right) \quad \text{on top surface} \quad (2)$$

$$-\nabla \phi \cdot \mathbf{n} = 0 \quad \text{on bottom surface and symmetry plane} \quad (3)$$

$$\phi = 0 \quad \text{on other surfaces} \quad (4)$$

where ϕ is the electric potential, σ the electric conductivity, I the current intensity, r_ϕ the Gaussian distribution radius of electric current density, r the radial distance to the frame origin and \mathbf{n} the outwards unit normal vector to the surface.

- Magnetostatic part:

The magnetic vector potential \mathbf{A} is derived from magnetic induction \mathbf{B} and defined as: $\mathbf{B} = \nabla \times \mathbf{A}$. Using the Lorentz gauge condition $\nabla \cdot \mathbf{A} = 0$ as a constraint, the magnetostatic part reads:

$$-\Delta \mathbf{A} = \mu_0 \mathbf{j} \quad (5)$$

with the boundary conditions:

$$\mathbf{A} \cdot \mathbf{n} = 0 \quad \text{on symmetry plane} \quad (6)$$

$$\mathbf{A} \times \mathbf{n} = \mathbf{0} \quad \text{on other surfaces} \quad (7)$$

where $\mathbf{j} = -\sigma \nabla \phi$ is the electric current density and μ_0 the magnetic permeability.

2.3 Heat transfer model

An enthalpy method [19, 20] is used to account for solid/liquid phase change, so the energy conservation equation reads:

$$\rho(\nabla h) \cdot (\mathbf{u} - \mathbf{u}_s) = \nabla \cdot \lambda \nabla T + s_{\text{Joule}} \quad (8)$$

where \mathbf{u} is the velocity in the fluid phase, \mathbf{u}_s the welding speed, ρ the density, h the enthalpy per unit mass, T the temperature, λ the thermal conductivity and $s_{\text{Joule}} = \mathbf{j} \cdot \mathbf{E}$ the volumetric heat source from the Joule effect, respectively. To take into account the

latent heat during phase change the enthalpy is calculated from specific heat as follows:

$$h(T) = \begin{cases} \int_{T_{\text{ref}}}^T c_{\text{ps}} dT & \text{if } T \leq T_s \\ \int_{T_{\text{ref}}}^{T_s} c_{\text{ps}} dT + f_1 L & \text{if } T_s < T \leq T_l \\ \int_{T_{\text{ref}}}^{T_s} c_{\text{ps}} dT + L + \int_{T_l}^T c_{\text{pl}} dT & \text{if } T_l < T \end{cases} \quad (9)$$

where T_{ref} is the reference temperature, L the latent heat of fusion/solidification and c_{ps} , c_{pl} the solidus and liquidus specific heat coefficients. The liquid metal fraction f_1 is assumed to vary linearly with temperature inside the mushy zone [21]:

$$f_1 = \begin{cases} 0 & \text{if } T \leq T_s \\ \frac{T - T_s}{T_l - T_s} & \text{if } T_s < T \leq T_l \\ 1 & \text{if } T > T_l \end{cases} \quad (10)$$

The boundary conditions are:

$$T = T_0 \quad \text{on inlet} \quad (11)$$

$$\lambda \nabla T \cdot \mathbf{n} = 0 \quad \text{on symmetry plane and outlet} \quad (12)$$

$$\lambda \nabla T \cdot \mathbf{n} = \mathbf{s}_{\text{Ray}} + \mathbf{s}_{\text{Cvs}} + \mathbf{s}_{\text{Sur}} \quad \text{on top surface} \quad (13)$$

$$\lambda \nabla T \cdot \mathbf{n} = \mathbf{s}_{\text{Ray}} + \mathbf{s}_{\text{Cvs}} \quad \text{on other surfaces.} \quad (14)$$

The radiative loss reads:

$$\mathbf{s}_{\text{Ray}} = -\epsilon \sigma_{\text{B}} (T^4 - T_{\infty}^4) \quad (15)$$

The convective heat loss reads:

$$\mathbf{s}_{\text{Cvs}} = -h_c (T - T_{\infty}) \quad (16)$$

Here ϵ is the emissivity of the assembly surfaces, h_c the convective heat transfer coefficient, σ_{B} the Stefan-Boltzmann constant and T_{∞} the ambient temperature. The surface heat source is modeled by a Gaussian distribution:

$$\mathbf{s}_{\text{Sur}} = \frac{UI\eta}{2\pi r_q^2} \exp\left(-\frac{r^2}{2r_q^2}\right) \quad (17)$$

with U the voltage, I the intensity, η the process efficiency, r the radial distance and r_q the radius of the Gaussian distribution of the surface heat source modeling the electric arc.

2.4 Incompressible fluid flow model

The heat transfer in the assembly is significantly dominated by advection in the melted pool. Therefore, the liquid metal fluid flow is modeled by the incompressible Navier-Stokes equations. The continuity and momentum equations read:

$$\nabla \cdot \mathbf{u} = 0 \quad (18)$$

$$\rho(\nabla \mathbf{u}) \cdot (\mathbf{u} - \mathbf{u}_s) = -\nabla p + \nabla \cdot \mu(\nabla \mathbf{u} + \nabla^t \mathbf{u}) + \mathbf{f}_{\text{Body}} + \mathbf{f}_{\text{Lor}} + \mathbf{f}_{\text{Ext}} \quad (19)$$

with the boundary conditions:

$$\mathbf{u} = \mathbf{u}_s \quad \text{on solid/liquid interface} \quad (20)$$

$$\mathbf{u} \cdot \mathbf{n} = 0 \quad \text{on top surface and symmetry plane} \quad (21)$$

$$(\mu(\nabla \mathbf{u} + \nabla^t \mathbf{u}) \cdot \mathbf{n}) \cdot \mathbf{t}_i = \mathbf{f}_{\text{Mar}} \cdot \mathbf{t}_i \quad (i = 1, 2) \quad \text{on top surface} \quad (22)$$

$$(\mu(\nabla \mathbf{u} + \nabla^t \mathbf{u}) \cdot \mathbf{n}) \cdot \mathbf{t}_i = 0 \quad (i = 1, 2) \quad \text{on symmetry plane} \quad (23)$$

where μ is the dynamic viscosity, \mathbf{t}_1 and \mathbf{t}_2 are two tangent vectors to the surface, and the driving forces in the melted pool are gravity (\mathbf{f}_{Body}), Lorentz force (\mathbf{f}_{Lor}) and Marangoni force (\mathbf{f}_{Mar}). These forces are expressed as:

$$\mathbf{f}_{\text{Body}} = \rho_{\text{ref}} \mathbf{g} [1 - \beta(T - T_{\text{ref}})] \quad (24)$$

$$\mathbf{f}_{\text{Lor}} = \mathbf{j} \times (\nabla \times \mathbf{A}) \quad (25)$$

$$\mathbf{f}_{\text{Ext}} = -c(1 - f_1)(\mathbf{u} - \mathbf{u}_s) \quad (26)$$

$$\mathbf{f}_{\text{Mar}} = \frac{\partial \gamma}{\partial T} \nabla_s T \quad (27)$$

where ∇_s is the tangential gradient operator defined as $\nabla - \mathbf{n}(\mathbf{n} \cdot \nabla)$. The surface tension gradient $\frac{\partial \gamma}{\partial T}$ depending on temperature and impurity composition of the steel was proposed by Sahoo [22]:

$$\frac{\partial \gamma(T, a_k)}{\partial T} = -A_g - R\Gamma_s \ln(1 + K a_k) - \frac{K a_k}{1 + K a_k} \times \frac{\Gamma_s \Delta H^0}{T} \quad (28)$$

with:

$$K(T) = k_1 \exp\left(-\frac{\Delta H^0}{RT}\right)$$

Here A_g is the opposite of $\frac{\partial \gamma}{\partial T}$ for a pure material, a_k the activity of the species k in the steel solution, R the universal gas constant, Γ_s the surface excess at saturation, k_1 a constant related to an entropy of segregation and ΔH^0 the standard heat of adsorption.

Free surface equation

Our goal is to simulate the shape of the weld pool in different welding positions. Therefore, the free surface of the melted pool is determined at steady state using the principle of minimization of the total potential energy [11]. The latter includes surface energy resulting from area change of the pool surface and work performed by arc pressure displacing the pool surface. The total potential energy minimization of the surface leads to the free surface equation [23]:

$$-p + [\mu(\nabla \mathbf{u} + \nabla^t \mathbf{u}) \cdot \mathbf{n}] \cdot \mathbf{n} = \frac{\gamma(T, a_k)}{R_1(z(x, y)) + R_2(z(x, y))} + \mathbf{f}_{\text{Arc}} \cdot \mathbf{n} \quad (29)$$

where x , y , z are the free surface coordinates ($z(x, y)$ is the free surface altitude), $R_1(z(x, y))$ and $R_2(z(x, y))$ are principal radii of curvature. The arc pressure is modeled by a Gaussian distribution:

$$\mathbf{f}_{\text{Arc}} = p_{\text{max}} \exp\left(-\frac{r^2}{2r_p^2}\right) \mathbf{n} \quad (30)$$

with p_{max} the maximum arc pressure, r the radial distance and r_p the characteristic radius of the arc pressure. The volume of the weld pool is kept constant during surface deformation, which leads to the following constraint and boundary conditions:

$$\int_S z(x, y) \, dx dy = 0 \quad \text{on the top surface (free surface)} \quad (31)$$

$$z(x, y) = 0 \quad \text{on the edge of the free surface} \quad (32)$$

3 Numerical model

3.1 Finite element model

The finite element method is used to discretize the electromagnetic, heat transfer and incompressible fluid flow equations of section 2. Quadratic approximation is used for the velocity field \mathbf{u} and geometry. Linear approximation is used for all the other field variables (ϕ , \mathbf{A} , p , h and T). The choice of quadratic finite element for velocity and geometry is dictated by an accurate representation of the free surface and the related physical phenomena (surface tension, Marangoni force) even on a coarse mesh. The choice of a linear interpolation for the pressure field ensures the stability of the velocity-pressure approximation. The choice of a linear interpolation for enthalpy, temperature, electric potential and magnetic potential is driven by considerations of computational cost and robustness. The method of weighted residual is applied to seek the cancellation of integral terms associated with our problem.

3.2 Solution strategy

The model involves a non-linear coupling between electromagnetism, heat transfer, fluid flow and free surface deformation. The non-linearities arise from convective terms in Navier-Stokes equations, radiative loss term in energy equation, phase change and the unknown melted pool shape. To handle this problem numerically, a segregated solution algorithm is used to compute the unknowns incrementally (Newton-like), as depicted in algorithm 1 implemented in the Cast3M finite element code [24]. The solution strategy is as follows: one computes first the electromagnetic fields, so that the Lorentz force is updated into the fluid flow equations together with the Joule effect in the heat transfer problem. Then, one computes the fluid flow with driving forces (Marangoni, Lorentz and buoyancy) weighted by an intensity factor f_α set to a starting value of 1%. Afterwards, the heat transfer problem and the free surface deformation problem are solved. Once convergence on the unknowns of the non-linear problem is obtained, the intensity factor f_α is gradually increased up to its nominal unit value. The process is then iterated until the convergence criteria are satisfied.

4 Validations: Comparison to experiments

To check our model capabilities, its computational results are compared with a representative set of experiments performed by Koudadje [10] for flat welding on 304L stainless steel with two sulfur contents (0.001 and 0.028 wt%). The computational domain is defined by its length $L_p = 100$ mm, width $2 \times W_p = 50$ mm and thickness $E_p = 18$ mm. The process parameters are the following: two welding speeds (15 and 30 cm·min⁻¹), welding current of 200 A, voltage of 15 V, process efficiency of $\eta = 0.68$, arc pressure of 200 N·m⁻² and the characteristic radius of the electric current $r_\phi = 2$ mm, heat source $r_q = 5$ mm and arc pressure $r_p = 1.18$ mm and simplified material properties of 304L stainless steel given in table 1 have been used.

Macrographs obtained in a perpendicular section to the weld bead are used as a basis of comparison. Table 2 presents the cross dimensions of melted pools obtained by Koudadje [10] and from our simulations. They reveal the influence of welding speed and sulfur content on the weld pool shape. Indeed, regardless of the sulfur content, increasing the welding speed results in decreasing the melted pool sizes (width and depth), as expected. Moreover, an increase of sulfur contents from 0.001 wt% to 0.028 wt% produces an increase of weld pool depth for both welding speeds (+25% for 15 cm·min⁻¹ and +15% for 30 cm·min⁻¹). For these comparisons the relative deviation between our model and Koudadje's experiments never exceeds 11.4% on the depth and 3.7% on the width of the weld pool.

Figure 2 shows the comparison between the experimental macrographs of Koudadje [10] and our numerical computations using an arc pressure of 200 N·m⁻². Based on these

comparisons, it turns out that our numerical model is able to reproduce relevant quantities of GTA welding. However, it appears that a better agreement is obtained for the low sulfur content (0.001 wt%) than for the high one (0.028 wt%), the latter being closer to the validity limit of Sahoo’s model [22].

5 Gravity effect in main welding configurations

Actual welding assembly may need to be performed in configurations other than flat requiring the welder to tune welding parameters in order to obtain a quality weld. Therefore, the influence of various welding positions with respect to gravity (flat (1G), horizontal (2G), vertical up (3G upward), vertical down (3G downward) and overhead (4G), depicted in figure 3) is numerically investigated and results are discussed in this section. The computational domain is one half plate of length $L_P = 100$ mm, width $W_P = 15$ mm and thickness $E_P = 10$ mm, at an initial temperature of 300 K. It is discretized with 250 000 finite elements, strongly refined in the weld pool region ($14 \text{ mm} \times 6 \text{ mm} \times 2.5 \text{ mm}$) located under the welding torch, where the finest mesh size is 8×10^{-5} m. In the present computations simplified material properties of 304L stainless steel reported in table 1 have been used. Prior to addressing this parametric study, the influence of free surface modeling (deformable or not) on the melted pool shape and sizes has been first considered on the classical configuration (1G).

5.1 Influence of free surface modeling

The free surface modeling is a key component in achieving accurate computations in GTA welding. To highlight this assertion computations have been performed for the following welding parameters: 304L stainless steel with 0.001 wt% of sulfur, welding speed of $15 \text{ cm} \cdot \text{min}^{-1}$, electric current of 150 A, voltage of 12 V, together with a process efficiency of $\eta = 0.68$ and an arc pressure of $200 \text{ N} \cdot \text{m}^{-2}$. Figure 4 shows the thermal field and weld pool limits computed with a non-deforming (left) and deforming (right) free surface. The free surface deformation only slightly impacts the thermal field (a 2% decrease in maximum temperature), but strongly affects the melted pool shape, plotted in figure 4 along the longitudinal symmetry plane (bottom left) and over the upper horizontal plane (bottom right). As expected, the melted pool is deeper with deforming free surface than in the not deforming case (a 33% increase). This result confirms the trends obtained by Kim [25] with a 2D axisymmetric calculation with constant surface tension coefficient. The melted pool is slightly shifted downstream and a little bit elongated (1.7% increase), whereas the maximum fluid flow velocity decreases by 8%. It is noteworthy, that even in this configuration, significant differences on the melted pool shape and sizes have been observed between the two free surface modeling, showing that a deformable free surface modeling is highly recommended to achieve accurate GTA welding computations.

5.2 Effect of welding positions

The considered welding configurations are depicted in figure 5 (bottom left) along with their related gravity directions (flat, horizontal, vertical up, vertical down and overhead). The computational domain can be restricted to one half of the plate when a symmetry exists along the longitudinal median plane (cases 1G, 3G downward, 3G upward and 4G), whereas for configuration (2G) no symmetry exists at all, so the full plate has to be considered. Moreover, to deal with weld pools of comparable sizes for the considered welding positions, the following welding parameters have been selected: sulfur content of 0.001 wt%, welding speed of $20 \text{ cm}\cdot\text{min}^{-1}$, arc pressure of $100 \text{ N}\cdot\text{m}^{-2}$, electric current of 150 A, voltage of 10 V and process efficiency of $\eta = 0.68$. Figure 5 shows the velocity field over the weld pool free surface and longitudinal symmetry plane for the five considered welding configurations. The welding position significantly influences the melted pool shape and particularly its free surface, but it does not change so much the fluid flow structure in the melted pool. Indeed, gravity mainly acts on the melted pool shape, whereas Marangoni and Lorentz forces drive the fluid flow. Figures 6, 7, 8 display the thermal field and the weld pool shapes for flat, overhead, vertical and horizontal configurations, respectively. The thermal field is only slightly impacted by the different positions (only 5% between flat and vertical-up cases). Gravity pulls the liquid metal from upper towards lower melted pool regions, so the weld pool free surface deforms in the gravity direction (3G down, 3G up, 2G cases) (figures 7, 8) resulting in a swelling of the bottom part of the pool.

Weld pool shapes are plotted in the longitudinal symmetrical plane in figures 6 and 7 for both flat, overhead and vertical down and up configurations, respectively. The weld bead shapes are quite similar in both 1G and 4G cases (figure 6), but the former is stable whereas the stability condition of the latter requires that surface tension forces balance gravity. In the vertical down position (3G down) welding and gravity directions give a convex deformation of the free surface below the welding torch because gravity tends to displace the melted pool towards the arc, unlike in other cases (figure 7 bottom left). Conversely, in the vertical up position (3G up) gravity drives the melted pool away from the arc, which causes a deeper weld pool (figure 7 bottom right). Similar trends were observed by Kumar [15] during Gas Metal Arc (GMA) welding. Relevant computed quantities are reported in table 3: for horizontal position (2G), the weld bead deformation is clearly asymmetrical about the horizontal median plane (widths of lower and upper parts of weld pool are 3.60 mm and 3.05 mm, respectively). A maximum depth of 1.27 mm is obtained in the vertical-up position (3G up).

6 Effect of the main operating parameters

Having discussed the influence of welding positions in section 5, let us now analyze the influence of some other leading welding parameters (welding speed, arc pressure and sulfur content) on the weld pool shape and fluid flow features. In this parametric study, the classical flat configuration is considered along with two sulfur contents (0.001, 0.03 wt%), two welding speeds (15, 30 cm·min⁻¹) and three arc pressures (100, 200 and 300 N·m⁻²). Current intensity, voltage and process efficiency are taken respectively equal to 150 A, 12 V and $\eta = 0.68$.

6.1 Welding speed influence

The influence of the welding speed on relevant computed quantities is reported in table 4. Doubling the welding speed from 15 cm·min⁻¹ to 30 cm·min⁻¹ with the same welding power reduces the weld pool size by roughly a factor of two, regardless of sulfur content. The weld pool volume is reduced from 49.26 mm³ to 25.70 mm³ with 0.001 wt% and from 56.14 mm³ to 29.14 mm³ with 0.03 wt%. This result is fully consistent with the related decrease in linear welding energy and is in good agreement with the experiments of Kong [26]. Figure 9 shows the weld pool shapes for the two sulfur contents and two welding speeds. For a given sulfur content, changing the welding speed does not alter the weld pool shape as the flow structure remains unchanged. This was also observed by Mills [27].

6.2 Arc pressure influence

The arc pressure depends on many welding parameters: electric current intensity, arc length, electrode geometry and shield gas. This arc pressure has a major influence on the free surface deformation and affects the weld pool depth. Its influence on the weld pool is studied for three arc pressures (100, 200 and 300 N·m⁻²) and constant welding energy (15 cm·min⁻¹, current intensity of 150 A, voltage of 12 V and $\eta = 0.68$ for process efficiency). Figure 10 displays the melted pool section in the longitudinal median plane for the three arc pressures and two sulfur contents (0.001 and 0.03 wt%). As the arc pressure increases the free surface deforms correspondingly and a trough forms below the torch along with a crest downstream. The free surface depression induces a comparable trough of the solid/liquid interface below the torch, but does not change the fluid flow structure. A close correlation between free surface depression and depth is also found by Ko [28]. For high sulfur content such as 0.03 wt%, arc pressure has a weaker effect on depth, as the weld pool deepens owing to the stronger centripetal flow (figure 10, right). Finally, arc pressure variation does not induce any volume change of molten pool: penetration increases while width decreases resulting in a constant melted volume.

6.3 Sulfur content influence

In arc welding of austenitic stainless steels, a few percent change in impurity quantity can strongly modify thermocapillary forces that drive the fluid flow, resulting in very different weld pool shape and size. In the present work, the surface tension coefficient is modeled by Sahoo’s model [22], which accounts for impurity contents (see Eq. (28)). Therefore the ability of our multiphysics model to reproduce welding of austenitic stainless steels has been investigated for two sulfur contents (0.001 and 0.03 wt%). For 0.001 wt%, the surface tension gradient $\partial\gamma/\partial T$ is always negative over the melted pool temperature range, whereas for 0.03 wt% it changes sign (positive value for $T < 2150$ K and negative above), reversing consequently both thermocapillary forces and fluid flow direction. The induced effect on the weld pool geometry is depicted in figure 11 (left), for a welding speed of $15 \text{ cm}\cdot\text{min}^{-1}$ and an arc pressure of $200 \text{ N}\cdot\text{m}^{-2}$ while relevant computed results are gathered in Table 4. An increase in sulfur content leads to an increase in depth and a decrease in weld pool length, which is in good agreement with the results of Koudadje [10] and Mishra [29]. The significant difference in melted pool shapes can be attributed to the flow structures induced by Marangoni forces. Indeed, for low sulfur content, the surface tension coefficient is negative which leads to a centrifugal flow. Two outward rotating vortices are present on both sides of the weld pool (figure 11 right bottom). Conversely, for high sulfur content, the surface tension coefficient is positive on the melted pool periphery, leading to a supplementary inward vortex (figure 11 right top).

7 Conclusion

A multiphysics numerical model devoted to compute relevant weldability characteristics (weld bead shape, penetration, etc.) has been developed for GTA welding. It is focused on the melted pool in order to account for its peculiar sensitivity to free surface deformations with respect to gravity, enabling us to simulate various welding positions. This model solves for the steady electromagnetic, continuity, momentum and energy equations taking into account free surface deformations and phase change, fluid flow velocity and weld pool shape. The free surface geometry is determined by minimizing the total potential energy of the weld pool, that enables to account for various welding position. A robust algorithm has been implemented to solve this highly challenging coupled nonlinear problem. The numerical model has been checked against experiments and it reproduces well the effects of sulfur contents and welding speeds on the melted pool shape and sizes. Then, computational results of parametric studies related to the welding positions, which constitutes the main novelty of this work, and to other leading welding parameters were presented. It turns out from our computations that accounting for free surface deformation leads to an increase in welding penetration and length

of weld pool along with a decrease in maximum temperature. The welding positions significantly affect the free surface deformation which deforms according to the gravity direction, but do not change the fluid flow direction. In the 2G case, the deformation of the melted pool is asymmetric with respect to the longitudinal median plane aligned with the electrode, which might lead to poor quality of the weld bead. For the considered welding conditions, the weld pool shapes are quite similar for cases 1G and 4G. However the stability of the latter is very weak, so this precludes from considering welding conditions that lead to wider melted pools in 4G. As previously reported by fixed free surface numerical models, an increase in welding speed reduces the weld pool sizes and volume, but this does not affect the weld bead geometry. An increase in arc pressure leads to more pronounced free surface deformations and a trough forms below the torch along with a crest downstream, particularly for low sulfur content. An increase of sulfur quantity causes an increase in penetration, a decrease in weld pool length, an increase in maximum temperature and a decrease in flow velocity.

Obviously, experimental verification of the effect of welding positions are greatly welcome to evaluate the predictive capabilities of our numerical model. But, in the meantime further work is on the way to account for metal filling and strong coupling with a 3D arc model in order to build a more comprehensive multiphysics model for GTA welding.

References

- [1] M. Tanaka, H. Terasaki, M. Ushio, and J. J. Lowke. A unified numerical modeling of stationary Tungsten-Inert-Gas welding process. *Metallurgical and materials transactions A*, 33(7):2043–2052, 2002.
- [2] M. Tanaka. An introduction to physical phenomena in arc welding processes. *Welding international*, 18(11):845–851, 2004.
- [3] H. G. Fan and R. Kovacevic. A unified model of transport phenomena in gas metal arc welding including electrode, arc plasma and molten pool. *Journal of Physics D: Applied Physics*, 37(18):2531–2544, 2004.
- [4] M. Brochard. *Modèle couplé cathode-plasma-pièce en vue de simulation du procédé de soudage à l'arc TIG (English title: A unified model of gas tungsten arc welding (GTAW) including electrode, arc plasma and molten pool)*. PhD thesis, Université de Provence (Aix-Marseille I) – CEA, 2009.
- [5] C. S. Wu, P. C. Zhao, and Y. M. Zhang. Numerical simulation of transient 3-D surface deformation of a completely penetrated GTA weld. *Welding journal*, 83(12):330s–335s, 2004.

- [6] P. C. Zhao, C. S. Wu, and Y. M. Zhang. Modelling the transient behaviours of a fully penetrated gas-tungsten arc weld pool with surface deformation. *Proceedings of the Institution of Mechanical Engineers, Part B: Journal of Engineering Manufacture*, 219(1):99–110, 2005.
- [7] W. Zhang, G. G. Roy, J. W. Elmer, and T. DebRoy. Modeling of heat transfer and fluid flow during gas tungsten arc spot welding of low carbon steel. *Journal of Applied Physics*, 93(5):3022–3033, 2003.
- [8] C. S. Wu and K. C. Tsao. Modelling the three-dimensional fluid flow and heat transfer in a moving weld pool. *Engineering computations*, 7(3):241–248, 1990.
- [9] T. Zacharia, S. A. David, J. M. Vitek, and T. DebRoy. Weld pool development during GTA and laser beam welding of type 304 stainless steel: Part II - Experimental correlation. *Welding Journal*, 68(12):510s–519s, 1989.
- [10] K. Koudadje. *Étude expérimentale et modélisation numérique du bain de fusion en soudage TIG d’aciers (English title: Experimental study and numerical modeling of weld pool in GTA welding of steels)*. PhD thesis, Université d’Aix-Marseille – EDF, 2013.
- [11] C. S. Wu, J. Chen, and Y. M. Zhang. Numerical analysis of both front- and back-side deformation of fully-penetrated GTAW weld pool surfaces. *Computational Materials Science*, 39(3):635–642, 2007.
- [12] J. H. Sun, C. S. Wu, and M. A. Chen. Numerical analysis of transient temperature field and keyhole geometry in controlled pulse key-holing plasma arc welding. *Numerical Heat Transfer, Part A: Applications*, 64(5):416–434, 2013.
- [13] T. Zhang, C. S. Wu, and Y. Feng. Numerical analysis of heat transfer and fluid flow in keyhole plasma arc welding. *Numerical Heat Transfer, Part A: Applications*, 60(8):685–698, 2011.
- [14] C. S. Wu, W. Zheng, and M. A. Chen. Improving the prediction accuracy of keyhole establishment time in plasma arc welding. *Numerical Heat Transfer, Part A: Applications*, 66(4):420–432, 2014.
- [15] A. Kumar and T. DebRoy. Heat transfer and fluid flow during gas-metal-arc fillet welding for various joint configurations and welding positions. *Metallurgical and Materials Transactions A*, 38(3):506–519, 2007.
- [16] M. L. Lin and T. W. Eagar. Influence of arc pressure on weld pool geometry. *Welding Journal*, 64(6):163s–169s, 1985.
- [17] W. H. Kim, H. G. Fan, and S. J. Na. Effect of various driving forces on heat and mass transfer in arc welding. *Numerical Heat Transfer, Part A Applications*, 32(6):633–652, 1997.

- [18] X. Kong, O. Asserin, S. Gounand, P. Gilles, J. M. Bergheau, and M. Medale. 3D finite element simulation of TIG weld pool. In *IOP Conference Series: Materials Science and Engineering*, volume 33. IOP Publishing, 2012.
- [19] B. Nedjar. An enthalpy-based finite element method for nonlinear heat problems involving phase change. *Computers & structures*, 80(1):9–21, 2002.
- [20] D. A. Knoll, D. B. Kothe, and B. Lally. A new nonlinear solution method for phase-change problems. *Numerical Heat Transfer: Part B: Fundamentals*, 35(4):439–459, 1999.
- [21] M. Medale, C. Touvrey, and R. Fabbro. An axi-symmetric thermo-hydraulic model to better understand spot laser welding. *European Journal of Computational Mechanics/Revue Européenne de Mécanique Numérique*, 17(5-7):795–806, 2008.
- [22] P. Sahoo, T. DebRoy, and M. J. McNallan. Surface tension of binary metal-surface active solute systems under conditions relevant to welding metallurgy. *Metallurgical transactions B*, 19(3):483–491, 1988.
- [23] M. C. Nguyen. *Modélisation et simulation multiphysique du bain de fusion en soudage à l’arc TIG (English title: Multiphysics modeling and numerical simulation of weld pool in GTA welding)*. PhD thesis, Université d’Aix-Marseille – CEA, 2015.
- [24] Cast3M software. *CEA Saclay*. Downloaded at: <http://www-cast3m.cea.fr/>, 2015.
- [25] S. D. Kim and S. J. Na. Effect of weld pool deformation on weld penetration in stationary gas tungsten arc welding. *Welding journal*, 71(5):179–193, 1992.
- [26] X. Kong. *Modélisation 3D d’écoulement avec surface libre pour le soudage à l’arc TIG (English title: 3D modeling of flow with free surface for GTA welding)*. PhD thesis, École Nationale d’Ingénieurs de Saint-Étienne – CEA, 2012.
- [27] K. C. Mills and B. J. Keene. Factors affecting variable weld penetration. *International Materials Reviews*, 35(1):185–216, 1990.
- [28] S. H. Ko, C. D. Yoo, and S. K. Choi. Effects of surface depression on pool convection and geometry in stationary GTAW. *Welding Journal(USA)*, 80(2):39s–45s, 2001.
- [29] S. Mishra, T. J. Lienert, M. Q. Johnson, and T. DebRoy. An experimental and theoretical study of gas tungsten arc welding of stainless steel plates with different sulfur concentrations. *Acta Materialia*, 56(9):2133–2146, 2008.

Tables

Symbol	Material property	Value
T_s	Solidus temperature	1673 K
T_l	Liquidus temperature	1723 K
T_{ref}	Reference temperature	1723 K
ρ_s	Solid phase density	$7500 \text{ kg}\cdot\text{m}^{-3}$
ρ_l	Liquid phase density	$6350 \text{ kg}\cdot\text{m}^{-3}$
c_{ps}	Specific heat of solid phase	$602 \text{ J}\cdot\text{kg}^{-1}\cdot\text{K}^{-1}$
c_{pl}	Specific heat of liquid phase	$720 \text{ J}\cdot\text{kg}^{-1}\cdot\text{K}^{-1}$
λ_s	Thermal conductivity of solid phase	$26 \text{ W}\cdot\text{m}^{-1}\cdot\text{K}^{-1}$
λ_l	Thermal conductivity of liquid phase	$20 \text{ W}\cdot\text{m}^{-1}\cdot\text{K}^{-1}$
L	Latent heat of fusion	$2.47 \times 10^5 \text{ J}\cdot\text{kg}^{-1}$
μ_l	Viscosity of liquid phase	$0.05 \text{ kg}\cdot\text{m}^{-1}\cdot\text{s}^{-1}$
h_c	Heat convection coefficient	$15 \text{ W}\cdot\text{m}^{-2}\cdot\text{K}^{-1}$
ϵ	Radiation emissivity	0.5
σ	Electrical conductivity	$7.7 \times 10^5 \text{ S}\cdot\text{m}^{-1}$
A_g	Opposite of $\partial\gamma/\partial T$ for a pure material	$4.3 \times 10^{-4} \text{ N}\cdot\text{m}^{-1}\cdot\text{K}^{-1}$
R	Gas constant	$8.3143 \text{ J}\cdot\text{mol}^{-1}\cdot\text{K}^{-1}$
ΔH^0	Standard heat of adsorption	$-1.66 \times 10^5 \text{ J}\cdot\text{kmol}^{-1}$
Γ_s	Surface excess at saturation	$1.3 \times 10^{-5} \text{ mol}\cdot\text{m}^{-2}$
γ_f	Surface tension at the melting temperature	$1.943 \text{ N}\cdot\text{m}^{-1}$
k_1	Entropy factor	3.18×10^{-3}
σ_B	Stefan-Boltzmann constant	$5.6704 \times 10^{-8} \text{ W}\cdot\text{m}^{-2}\cdot\text{K}^{-4}$

Table 1: Material properties of 304L stainless steel used in this work [17, 22].

[S] (wt%)	0.001		0.001		0.028		0.028	
u_s (cm·min ⁻¹)	15		30		15		30	
Weld pool envelope	Width (mm)	Depth (mm)	Width (mm)	Depth (mm)	Width (mm)	Depth (mm)	Width (mm)	Depth (mm)
Experiment (E)	9.4±0.4	1.7±0.2	7.7±0.4	1.3±0.2	9.8±0.4	2.1±0.2	7.5±0.4	1.5±0.2
Simulation (S)	9.40	1.52	7.61	1.28	9.44	1.86	7.62	1.37
Deviation $\left(\frac{S-E}{E}\right)$	0.0%	-10.6%	-1.2%	-1.5%	-3.7%	-11.4%	1.6%	-8.7%

Table 2: Comparison of the weld pool sizes from experiments of Koudadje [10] and present numerical model.

Case	T_{\max} (K)	$\ \mathbf{u}\ _{\max}$ (m·s ⁻¹)	Length (mm)	Width (mm)	Depth (mm)	Volume (mm ³)
1G	2425	0.21	7.34	6.24	0.83	22.18
2G	2421	0.19	8.54	3.60 + 3.05	0.92	36.44
3G upward	2308	0.25	7.65	6.02	1.27	25.64
3G downward	2385	0.19	7.12	6.72	1.06	20.80
4G	2398	0.20	7.44	6.26	0.96	22.94

Table 3: Relevant computed quantities related to the weld pool for various welding positions.

[S] (wt%)	\mathbf{u}_s (cm·min ⁻¹)	T_{\max} (K)	$\ \mathbf{u}\ _{\max}$ (m·s ⁻¹)	Length (mm)	Width (mm)	Depth (mm)	Volume (mm ³)
0.001	15	2525	0.26	9.66	8.02	1.26	49.26
0.001	30	2467	0.23	8.17	6.42	0.99	25.70
0.03	15	2680	0.19	8.74	7.96	1.51	56.14
0.03	30	2598	0.17	7.73	6.34	1.09	29.14

Table 4: Relevant computed quantities for two welding speeds and two sulfur contents (arc pressure is 200 N·m⁻² and welding energy is $\eta UI = 612$ W).

Figure captions

Figure 1: Sketch of computational domain geometry.

Figure 2: Comparison of weld bead macrographs from Koudadje [10] with our computations (red lines) using Sahoo's model [22] for two sulfur contents and two welding speeds.

Figure 3: Welding positions considered in this work.

Figure 4: Thermal field and longitudinal section and top view of the weld pool shape with and without free surface deformation for 304L stainless steel with 0.001 wt% of sulfur content.

Figure 5: Gravity direction and related velocity field in the weld pool for the considered welding configurations.

Figure 6: Thermal field (K) and weld pool limit for flat (1G) and overhead (4G) cases. Comparison of the weld pool shapes in the longitudinal section.

Figure 7: Thermal field (K) and weld pool limit for vertical down (3G down) and vertical up (3G up) cases. Comparison of weld pool shapes in the longitudinal section with the flat case (1G).

Figure 8: Thermal field (K) for horizontal case (2G), side views from right (left) and left (right).

Figure 9: Weld pool shapes for two sulfur contents (0.001 wt%, left and 0.03 wt%, right) and two welding speeds ($15 \text{ cm}\cdot\text{min}^{-1}$, blue line and $30 \text{ cm}\cdot\text{min}^{-1}$, red line). The arrow length of the x, y, z -axis corresponds to 1 mm.

Figure 10: Weld pool section in longitudinal median plane for three arc pressures and 0.001 wt% (left) and 0.03 wt% (right) sulfur content.

Figure 11: Molten pool shapes for two sulfur contents (left): 0.001 wt% (blue line) and 0.03 wt% (red line). Velocity field (right) in longitudinal section (xz -plane) of the melt pool for these two values. The length of the arrows of the x, y, z -axis corresponds to 1 mm.

Figures

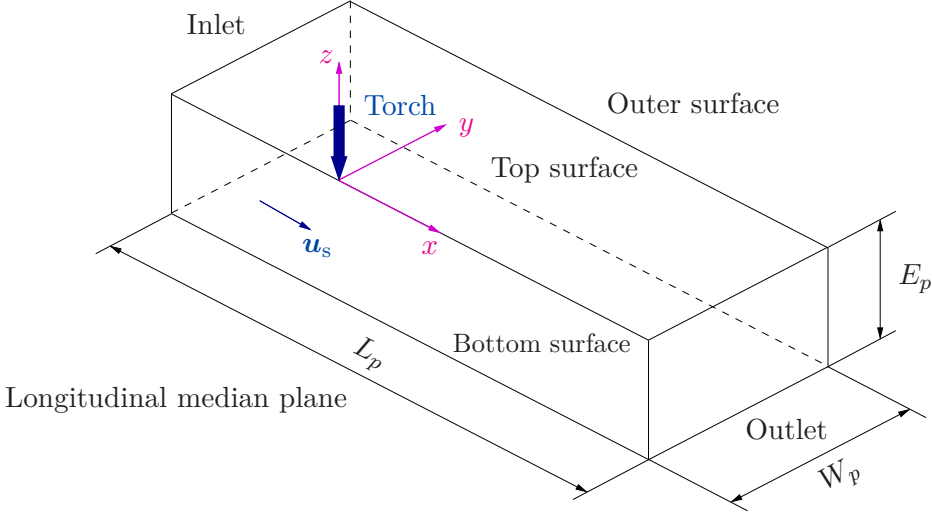
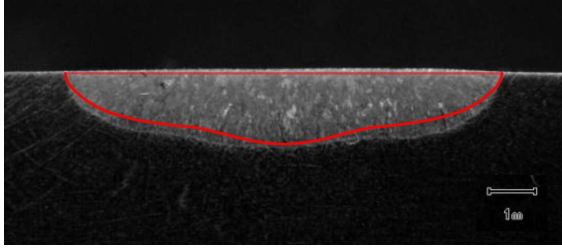
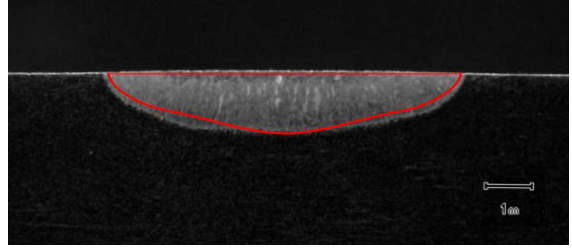


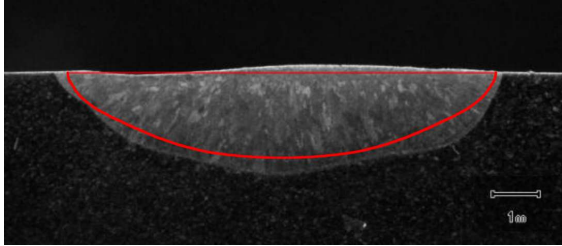
Figure 1: Sketch of computational domain geometry.



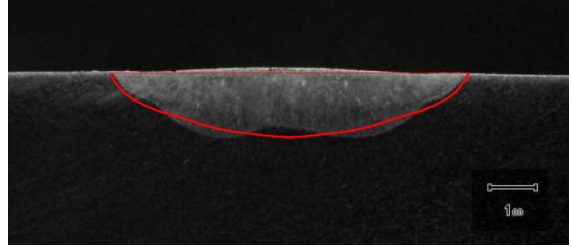
(a) 0.001 wt% sulfur, $u_s = 15 \text{ cm}\cdot\text{min}^{-1}$



(b) 0.001 wt% sulfur, $u_s = 30 \text{ cm}\cdot\text{min}^{-1}$



(c) 0.028 wt% sulfur, $u_s = 15 \text{ cm}\cdot\text{min}^{-1}$



(d) 0.028 wt% sulfur, $u_s = 30 \text{ cm}\cdot\text{min}^{-1}$

Figure 2: Comparison of weld bead macrographs from Koudadje [10] with our computations (red lines) using Sahoo's model [22] for two sulfur contents and two welding speeds.

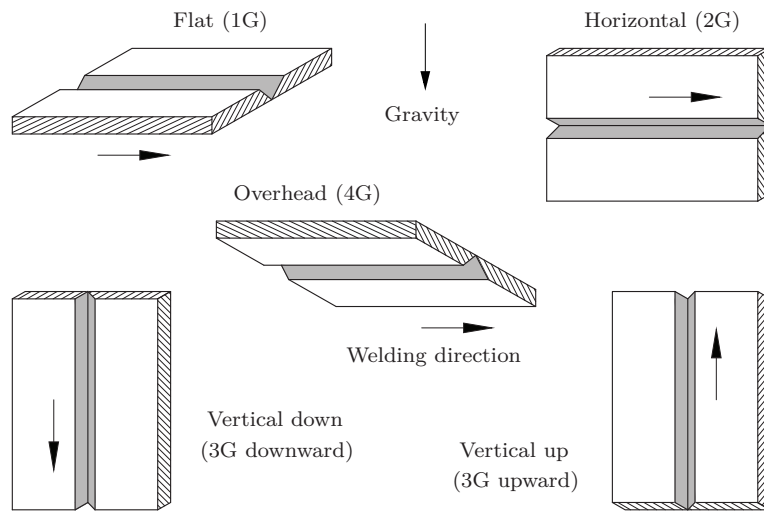


Figure 3: Welding positions considered in this work.

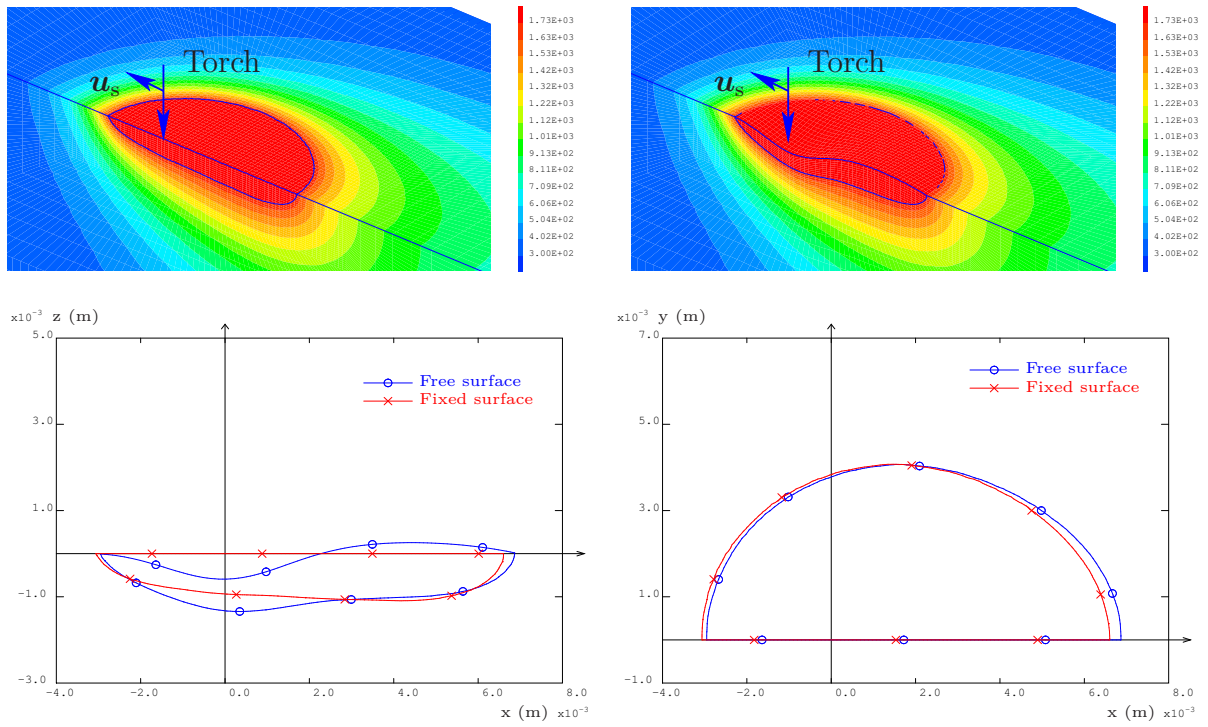


Figure 4: Thermal field (K) and longitudinal section and top view of the weld pool shape with and without free surface deformation for 304L stainless steel with 0.001 wt% of sulfur content.

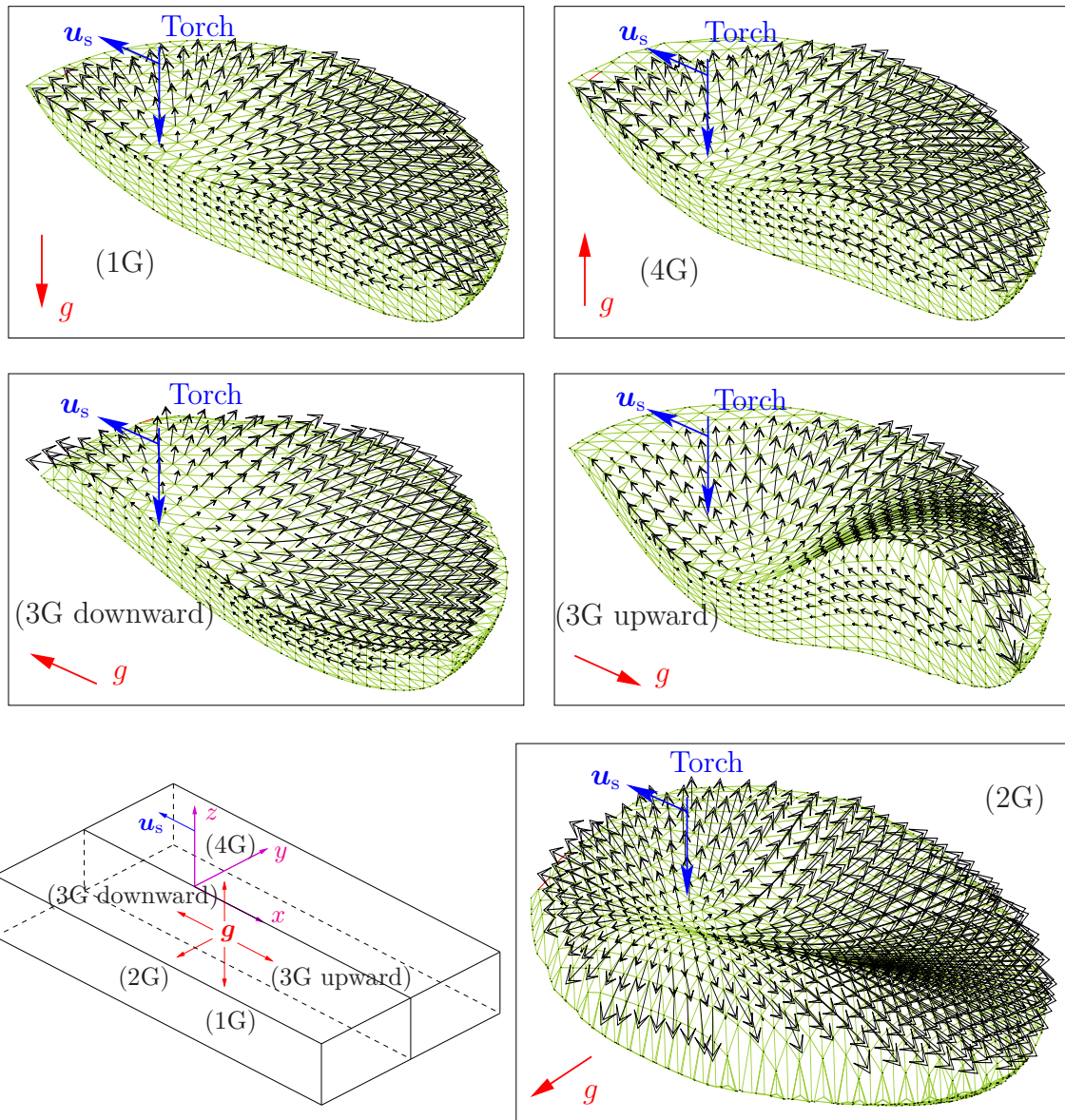


Figure 5: Gravity direction and related velocity field in the weld pool for the considered welding configurations.

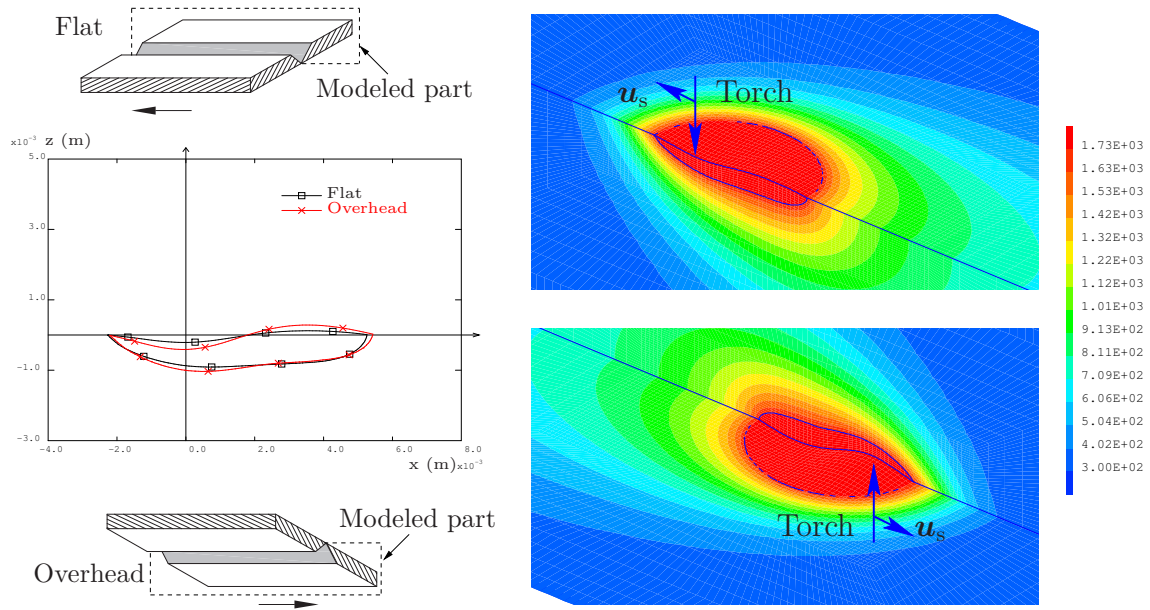


Figure 6: Thermal field (K) and weld pool limit for flat (1G) and overhead (4G) cases. Comparison of the weld pool shapes in the longitudinal section.

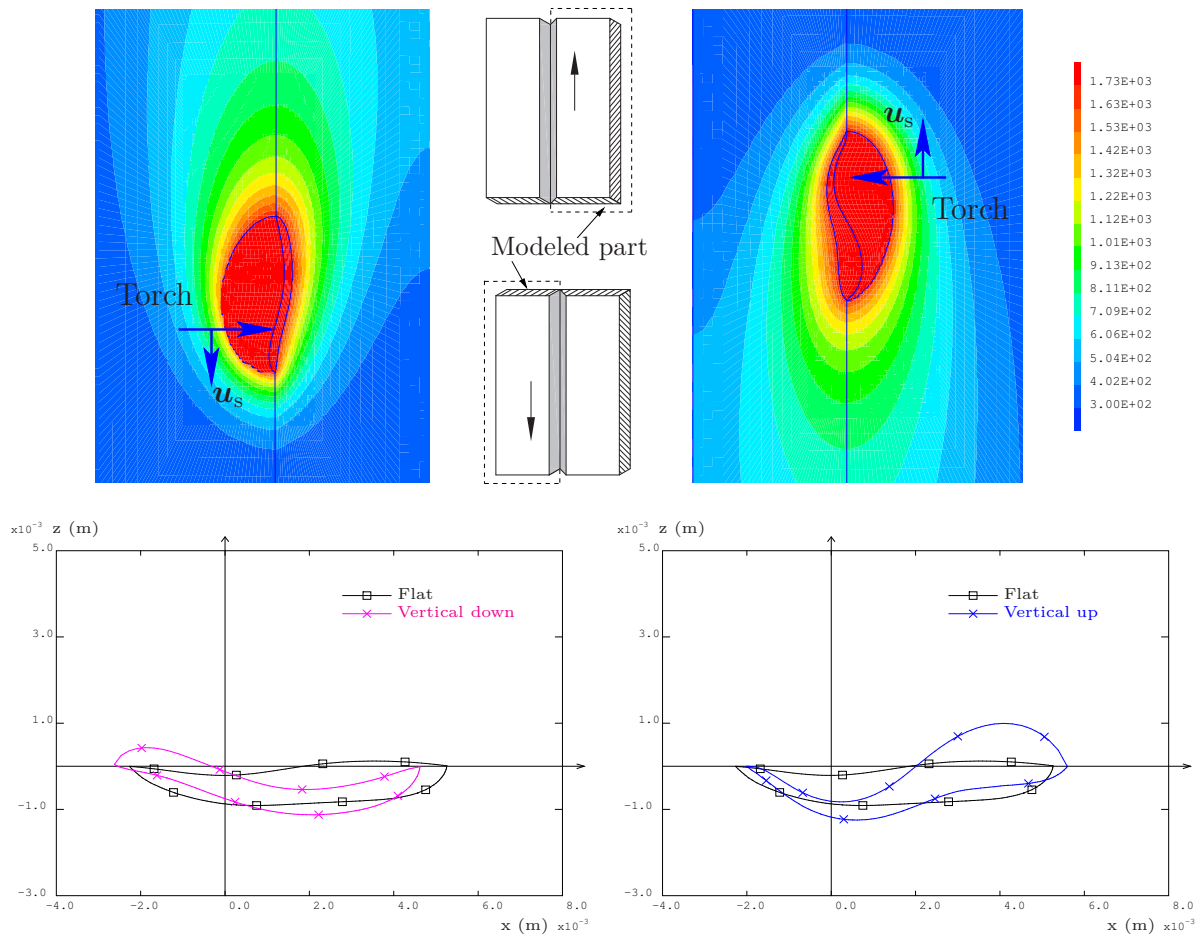


Figure 7: Thermal field (K) and weld pool limit for vertical down (3G down) and vertical up (3G up) cases. Comparison of weld pool shapes in the longitudinal section with the flat case (1G).

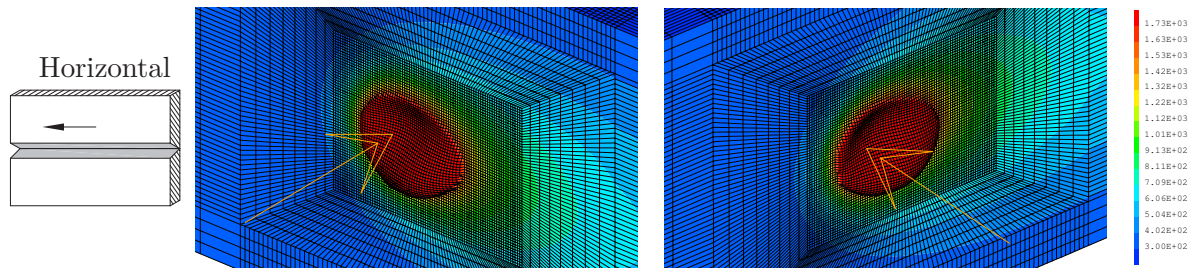


Figure 8: Thermal field (K) for horizontal case (2G), side views from right (left) and left (right).

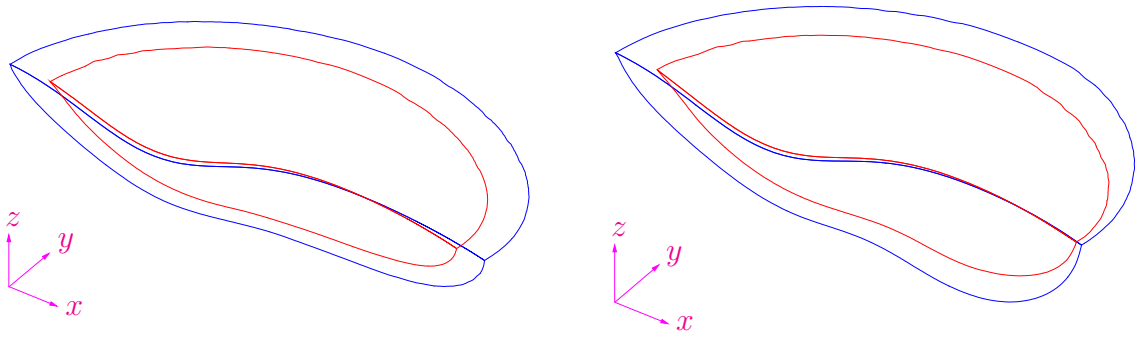


Figure 9: Weld pool shapes for two sulfur contents ($0.001 \text{ wt}\%$, left and $0.03 \text{ wt}\%$, right) and two welding speeds ($15 \text{ cm}\cdot\text{min}^{-1}$, blue line and $30 \text{ cm}\cdot\text{min}^{-1}$, red line). The arrow length of the x, y, z -axis corresponds to 1 mm .

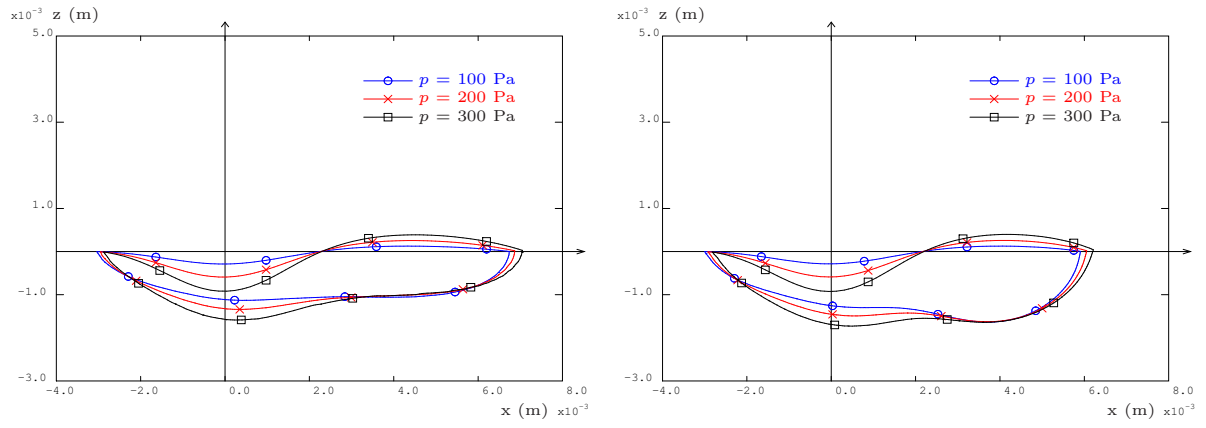


Figure 10: Weld pool section in longitudinal median plane for three arc pressures and 0.001 wt% (left) and 0.03 wt% (right) sulfur content.

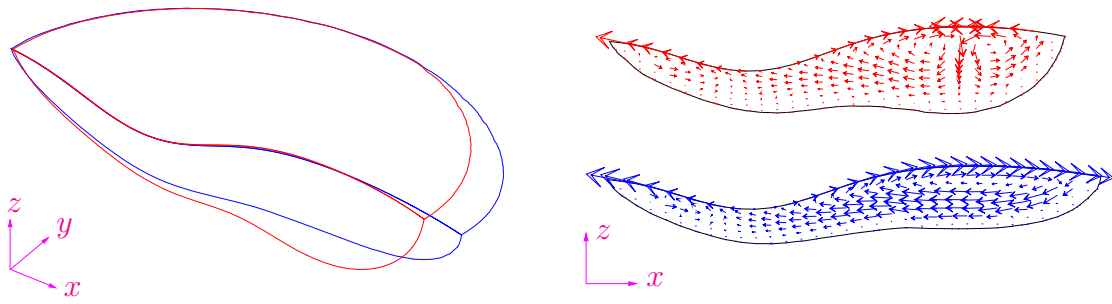


Figure 11: Molten pool shapes for two sulfur contents (left): 0.001 wt% (blue line) and 0.03 wt% (red line). Velocity field (right) in longitudinal section (xz -plane) of the melt pool for these two values. The length of the arrows of the x, y, z -axis corresponds to 1 mm.

Algorithm

Algorithm 1 Solution algorithm of the coupled non-linear problem

Initial conditions: $(\phi, \mathbf{A}, \mathbf{u}, p, z, h, T, \alpha, f_\alpha, \delta_{\text{conv}})^0$ at $i = 0$

repeat

$i \leftarrow i + 1$

1. Determination of the melted pool shape (characterized by $T > T_s$)

2. Calculation of electromagnetic fields (ϕ^i, \mathbf{A}^i)

3. Calculation of fluid flow increments $(\delta_{\mathbf{u}}, \delta_p)$ and update $(\mathbf{u}, p)^i = (\mathbf{u}, p)^{i-1} + (\delta_{\mathbf{u}}, \delta_p)$

4. Calculation of free surface increment δ_z , update $z^i = z^{i-1} + \delta_z$ and mesh movement

5. Calculation of enthalpy increment δ_h , update $h^i = h^{i-1} + \delta_h$,

calculation $T^i = T(h^i)$, δT and update coefficients depending on the temperature T^i

if $\delta_{\text{inc}} = \max\|(\delta_{\mathbf{u}}, \delta z, \delta T)\| < \delta_{\text{conv}}$ (Convergence?) **then**

$\alpha \leftarrow \min(\alpha \times f_\alpha, 1)$ (increase of the driving forces)

end if

until $(\delta_{\text{inc}} < \delta_{\text{conv}}$ and $\alpha = 1)$ or $i > i_{\text{max}}$
